


Non-Bloch \mathcal{PT} symmetry and topological phase transition in one-dimensional nonreciprocal topoelectrical circuits

Xiao-Feng Nie,¹ Ye-Wei-Yi Li,¹ Wen-Xue Cui^{1,2,*}, Shou Zhang,^{1,†} and Hong-Fu Wang^{1,‡}

¹*Department of Physics, College of Science, Yanbian University, Yanji, Jilin 133002, China*

²*State Key Laboratory of Surface Physics and Department of Physics, Fudan University, Shanghai 200433, China*

 (Received 15 October 2023; revised 15 January 2024; accepted 6 February 2024; published 26 February 2024)

We propose a feasible scheme to implement a one-dimensional non-Hermitian Su-Schrieffer-Heeger model with long-range hopping using the electrical circuit system. We investigate the admittance spectrum and node voltage density distribution of the current system. The non-Bloch \mathcal{PT} symmetry and its breaking can be effectively demonstrated using the saddle point theory and the ratio of complex eigenenergy. It is important to note that the phase boundary of non-Bloch \mathcal{PT} symmetry is solely determined by the long-range hopping strengths. Moreover, we observe that the system exhibits zero-admittance topological end and gap modes with varying strength relations between intercell and long-range hopping. We further represent the winding number phase diagram, which reveals the distinct topological phase transition from $w = \pm 1$ to $w = 0$. Our work provides a method to simulate nonreciprocal topoelectrical circuits and contributes to understanding the interplay between topology and non-Hermiticity.

DOI: [10.1103/PhysRevA.109.022241](https://doi.org/10.1103/PhysRevA.109.022241)

I. INTRODUCTION

As a complex extension of conventional Hermitian systems, non-Hermitian systems have gained significant attention due to their widespread applications in condensed-matter physics, which have been used to investigate the wave systems with gain and loss [1–5], open systems [6–11], finite quasi-particle lifetimes [12–14], and topological lasing [15–19]. Non-Hermitian systems exhibit unique characteristics that can possess nonorthogonal eigenvectors [20,21], exceptional points [22–25], and skin effect [26–30]. Unlike Hermitian systems, the eigenenergy spectrum of non-Hermitian systems has complex energy due to the lack of Hermitian conjugate symmetry of the Hamiltonian. This complex spectrum adds a layer of richness and complexity to the study of non-Hermitian systems. Non-Hermitian systems have led to the revision of the bulk-boundary correspondence [26,31–33], the introduction of new topological invariants [26,34,35], and the exploration of the generalized Brillouin zone (GBZ) [26,36–42]. To enhance the theoretical framework of the GBZ, the concept of the auxiliary GBZ has been proposed as a method to calculate analytical solutions of the GBZ [30,41,43–45], providing a valuable tool for studying the properties and behavior of non-Hermitian systems.

However, even though the Hamiltonian does not possess Hermitian conjugate symmetry in systems with \mathcal{PT} symmetry, it still exhibits a purely real eigenenergy spectrum. This counterintuitive phenomenon has been extensively studied and exploited in various fields of research [46–50]. In contrast,

the non-Hermitian systems composed of nonreciprocal elements, although lacking \mathcal{PT} symmetry, can still hold a purely real eigenenergy spectrum under the open boundary condition (OBC), which is connected by the non-Bloch \mathcal{PT} -symmetry theory [51]. The non-Bloch \mathcal{PT} symmetry and its breaking can be determined using saddle point theory [43,51]. These methods contribute to our understanding of the occurrence of purely real eigenenergy in non-Hermitian systems. Moreover, the study of non-Hermitian systems induced by nonreciprocity has been extensively explored in various platforms. Among them, the electric circuit network is one of the most promising platforms to realize quantum simulation by the advantages of controllability and flexibility in modulating coupling coefficients [25,52–55]. This advantage is particularly pronounced in the context of the condensed-matter tight-binding lattice systems, where the mode and strength of couplings would ultimately determine the topological properties of the system. As a result, topological electric circuit networks have earned significant attention and have been widely studied theoretically and experimentally.

Inspired by the above work, we propose a feasible scheme to simulate the nonreciprocal Su-Schrieffer-Heeger (SSH) model with long-range hopping with electrical circuits consisting of capacitors, inductors, and operational amplifiers. The nonreciprocal coupling between two nodes can be realized using an operational-amplifier-based negative impedance converter with current inversion. We investigate the non-Bloch \mathcal{PT} symmetry of the system by analyzing the motion of the saddle points. The non-Bloch \mathcal{PT} -symmetry phase boundary is given by the ratio of the complex eigenenergies. Notably, the phase boundary of non-Bloch \mathcal{PT} symmetry is solely determined by the long-range hopping strengths C_4 and C_5 . Through the numerical calculation of the admittance spectrum and node voltage density distribution, we

*cuiwenxue@ybu.edu.cn

†szhang@ybu.edu.cn

‡hfwang@ybu.edu.cn

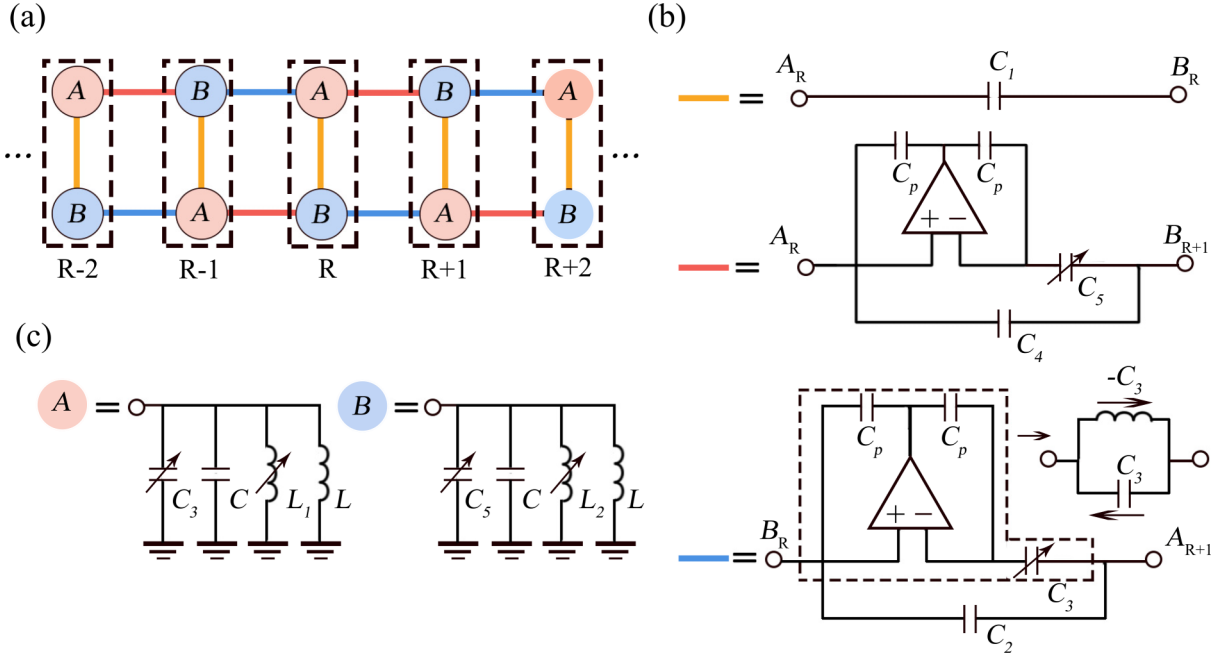


FIG. 1. Sketch of 1D nonreciprocal topoelectrical circuit consisting of operational amplifiers, inductors, and capacitors, designed to simulate a non-Hermitian SSH model with long-range hopping. (a) The dashed box indicates a unit cell with two nodes A and B . R is the unit cell index. (b) Different types of couplings between the nodes. The yellow, red, and blue lines represent the intracell, long-range, and intercell hopping, respectively. And the dashed box is the negative impedance converter, and it can be approximated as a capacitor of C_3 pointing left and an inductor of $-C_3$ pointing right. (c) Grounding mechanism of electrical nodes. The inductors L and $L_{1,(2)}$ and the capacitors $C_{3,(5)}$ can be used to eliminate the diagonal terms of the matrix H .

observe the presence of zero-admittance topological end and gap modes in the current system. For $C_2 > C_4$, it is found that there exists topological phase transitions with winding numbers from $w = 1$ to $w = 0$ in both the non-Bloch \mathcal{PT} -symmetry unbroken and broken regions. Furthermore, the topological zero-admittance end modes are localized at the first (or last) site. For $C_2 < C_4$, the system has the topological phase transition with the winding number from $w = -1$ to $w = 0$, and the topological zero-admittance gap modes are localized at the second (or penultimate) site, which is a significant difference compared to the case of $C_2 > C_4$.

This paper is organized as follows. In Sec. II, we give the model and Hamiltonian of the system. In Sec. III, we investigate in detail the relation of topological and non-Hermitian properties of the current system in different strength relations between the intercell and long-range hopping. Finally, a conclusion is given in Sec. IV.

II. MODEL AND HAMILTONIAN

As shown in Fig. 1, we consider a one-dimensional (1D) nonreciprocal electrical circuit composed of capacitors, inductors, and operational amplifiers, where each unit cell contains two electrical nodes A and B depicted by the dashed box. The intracell coupling mode is reciprocal, which can be achieved by controlling the capacitors. The nonreciprocal coupling of intercells can be realized using a negative impedance converter, with $C_{i \rightarrow j} = -C_{j \rightarrow i}$. By paralleling the negative impedance converter with a capacitor, we can achieve

adjustable nonreciprocal coupling modes, as shown in Fig. 1(b). For simplicity, we only consider positive coupling strengths except for the nonreciprocal terms. In Fig. 1(c), the nodes are connected to the ground through a common inductor L and a common capacitor C . The nodes A require an additional parallel connection with the variable capacitor C_3 and the variable inductor L_1 , and nodes B require a connection with the variable capacitor C_5 and the variable inductor L_2 . The voltages of the nodes are governed by Kirchhoff's current law and the net current satisfying $I_A = I_B = 0$. We obtain the expression for the admittance of the common capacitor C as follows [55]:

$$\begin{aligned} CV_{A,R} &= g_A V_{A,R} + C_1 V_{B,R} + (C_2 - C_3) V_{B,R-1} \\ &\quad + (C_4 + C_5) V_{B,R+1}, \\ CV_{B,R} &= g_B V_{B,R} + C_1 V_{A,R} + (C_2 + C_3) V_{A,R+1} \\ &\quad + (C_4 - C_5) V_{A,R-1}, \end{aligned} \quad (1)$$

where $g_{A,B} = (\frac{1}{w^2 L} - C_1 - C_2 - C_4) + (\frac{1}{w^2 L_{1,2}} - C_{5,3})$, it can be written in the form of

$$HV = CV, \quad (2)$$

which is the nonreciprocal electric circuit equivalent of the Schrödinger equation $H|\phi\rangle = E|\phi\rangle$, where the matrix H , the admittance eigenvalues C , and node voltages V represent the Hamiltonian matrix H , eigenenergies E , and eigenstates $|\phi\rangle$, respectively. V is written as $V = (V_{A,1}, V_{B,1}, V_{A,2}, V_{B,2}, \dots, V_{A,L}, V_{B,L})^T$ and H is the matrix

constructed on the right side of Eq. (1) with

$$H = \begin{bmatrix} g_A & C_1 & 0 & C_4 + C_5 & \dots \\ C_1 & g_B & C_2 + C_3 & 0 & \dots \\ 0 & C_2 - C_3 & g_A & C_1 & \dots \\ C_4 - C_5 & 0 & C_1 & g_B & \dots \\ \vdots & \vdots & \vdots & \vdots & \ddots \end{bmatrix}. \quad (3)$$

When performing the following settings of the resonant frequency with $w = 1/\sqrt{L(C_1 + C_2 + C_4)}$ and when the variable inductors satisfy $L_{1,2} = 1/(w^2 C_{5,3})$, the current system is equivalent to a non-Hermitian SSH model with long-range nonreciprocal hopping, which is described by

$$H = \sum_j [C_1(a_{j,A}^\dagger a_{j,B} + a_{j,B}^\dagger a_{j,A}) + (C_2 - C_3)a_{j+1,A}^\dagger a_{j,B} + (C_2 + C_3)a_{j,B}^\dagger a_{j+1,A} + (C_4 - C_5)a_{j+1,B}^\dagger a_{j,A} + (C_4 + C_5)a_{j,A}^\dagger a_{j+1,B}], \quad (4)$$

where C_1 is the intracell hopping strength, $C_2 \pm C_3$ is the intercell nonreciprocal hopping strength, and $C_4 \pm C_5$ is the long-range nonreciprocal hopping strength. Since the periodic arrangement of the current electric circuit, the system satisfies the Bloch theorem $V_{A,B}(R+r) = e^{i\vec{k}\cdot\vec{r}} V_{A,B}(R)$. By applying the Fourier transformations, the Hamiltonian of the system in momentum space can be written as

$$H(k) = \begin{bmatrix} 0 & h_+(k) \\ h_-(k) & 0 \end{bmatrix}, \quad (5)$$

where $h_{\pm}(k) = C_1 + (C_2 \mp C_3)e^{\mp ik} + (C_4 \pm C_5)e^{\pm ik}$. The current system holds the chiral symmetry with the relation $\sigma_z H(k) \sigma_z = -H(k)$.

We can construct a diagonal matrix to transform H into a Hermitian matrix with a similarity transformation $S^{-1}HS = \tilde{H}$ [26,46], where $S = \text{diag}(1, 1, r, r, r^2, r^2, \dots, r^L, r^L)$ and r satisfies

$$r = \sqrt{\frac{C_4 - C_5}{C_4 + C_5}}. \quad (6)$$

Under the above similarity transformation operation, we require that nonreciprocal strengths C_3 and C_5 satisfy

$$C_3 = \frac{C_2}{C_4} C_5. \quad (7)$$

Moreover, as both C_3 and C_5 are variable capacitors in the current electrical circuit, we set C_5 in the form of

$$C_5 = J \cos \theta, \quad (8)$$

where θ represents the modulation phase. In the current topoelectrical circuits, all couplings are implemented via capacitors to ensure positive hopping strengths. To achieve sign inversion for nonreciprocal terms, a negative impedance converter can be utilized. The corresponding Hamiltonian \tilde{H} of the system is written as

$$\tilde{H}(k) = \begin{bmatrix} 0 & C_1 + \tilde{C}_2 e^{-ik} + \tilde{C}_4 e^{ik} \\ C_1 + \tilde{C}_2 e^{ik} + \tilde{C}_4 e^{-ik} & 0 \end{bmatrix}, \quad (9)$$

where $\tilde{C}_4 = \sqrt{(C_4 - C_5)(C_4 + C_5)}$ and $\tilde{C}_2 = C_2 \tilde{C}_4 / C_4$. The non-Hermitian H becomes Hermitian for $|C_5| < C_4$ and remains non-Hermitian for $|C_5| > C_4$ because r becomes purely imaginary. According to Eq. (9), the topological phase transition of the system occurs at $k = \pm\pi$ for $C_1 = \tilde{C}_2 + \tilde{C}_4$ and at $k = 0$ for $C_1 = -(\tilde{C}_2 + \tilde{C}_4)$, namely,

$$C_5 = \pm C_4 \sqrt{1 - \frac{C_1^2}{(C_2 + C_4)^2}}. \quad (10)$$

For this corresponding non-Hermitian \tilde{H} , as \tilde{C}_2 and \tilde{C}_4 are purely imaginary, we need to perform $\tilde{C}_2 \rightarrow i|\tilde{C}_2|$ and $\tilde{C}_4 \rightarrow i|\tilde{C}_4|$. Then, we can obtain the eigenvalues of \tilde{H} , which are given as

$$E_{\pm}(k) = \pm \sqrt{f(k)},$$

$$\text{Im}[f(k)] = 2iC_1(|\tilde{C}_2| + |\tilde{C}_4|) \cos k,$$

$$\text{Re}[f(k)] = C_1^2 - (|\tilde{C}_2|^2 + |\tilde{C}_4|^2 + 2|\tilde{C}_2||\tilde{C}_4| \cos 2k). \quad (11)$$

After solving $E_{\pm}(k) = 0$, with $k = \pm\pi/2$, the topological phase transition occurs at $C_1 = \pm(|\tilde{C}_2| - |\tilde{C}_4|)$, namely,

$$C_5 = \pm C_4 \sqrt{1 + \frac{C_1^2}{(C_2 - C_4)^2}}. \quad (12)$$

According to the previous discussion, the presence of the Hermitian Hamiltonian \tilde{H} indicates the existence of a purely real spectrum, corresponding to the non-Bloch \mathcal{PT} -symmetry unbroken phase. Conversely, the non-Hermitian Hamiltonian \tilde{H} signifies a non-Bloch \mathcal{PT} -symmetry broken phase. Inspired by the above idea, we discuss the non-Bloch \mathcal{PT} symmetry and the topological phase transition in the next section.

III. RESULTS AND DISCUSSIONS

A. Non-Bloch \mathcal{PT} symmetry

As shown in Figs. 2(a) and 2(b), we plot the admittance spectrum as a function of θ under the OBC with $C_1 = 0.6$ mF, $C_2 = 1$ mF, $C_4 = 0.5$ mF, $J = 1$ mF, and $N = 160$. We find the system holds a pure real spectrum in the region of $\theta \in (\pi/3, 2\pi/3) \cup (4\pi/3, 5\pi/3)$, corresponding to the non-Bloch \mathcal{PT} -symmetry unbroken phase. However, for $\theta \in (0, \pi/3) \cup (2\pi/3, 4\pi/3) \cup (5\pi/3, 2\pi)$, the system holds complex eigenvalues associated with the non-Bloch \mathcal{PT} -symmetry broken phase. Since we can define that the non-Bloch \mathcal{PT} -symmetry broken phase is associated with the change in Hermiticity of \tilde{H} . The coalescence of saddle point energies can verify the non-Bloch \mathcal{PT} symmetry and its breaking discussed above. In this theory, we need to replace the usual Bloch phase factor e^{ik} with $\beta = re^{ik}$, and solve the equations $f(\beta, E) \equiv \det[H(\beta) - E] = 0$ and $\partial_{\beta} f(\beta, E) = 0$ to get all the information about the saddle points. The ends of the OBC bulk spectrum always correspond to the saddle points, and the saddle points belong to the GBZ.

We first aim at the saddle points on the complex energy plane, as shown in Figs. 3(a)–3(c). It is found that two pairs of saddle point energies, S_1 and S_2 , and S_3 and S_4 , are located at the ends of the energy band in Fig. 3(a). With the increase of C_5 , the energy bands gradually shrink, and two pairs of

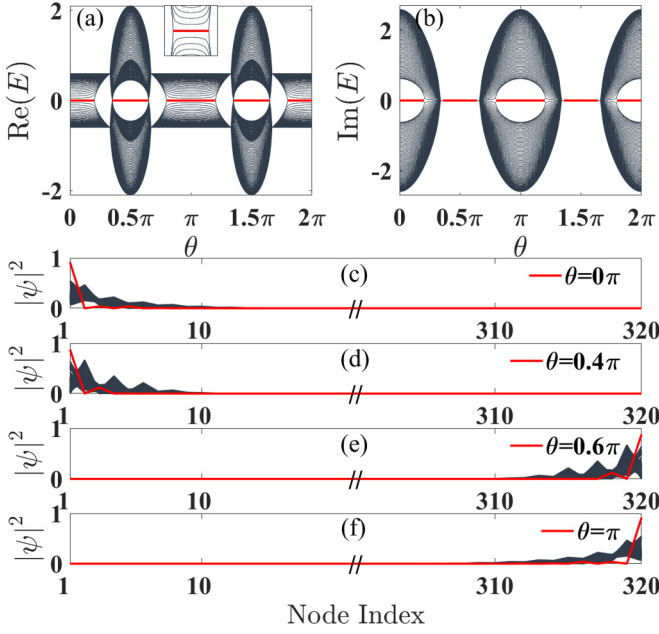


FIG. 2. Admittance spectrum of H as a function θ under the OBC with real (a) and imaginary (b) spectra. Node voltage density distribution of the system with (c) $\theta = 0$, (d) $\theta = 0.4\pi$, (e) $\theta = 0.6\pi$, and (f) $\theta = \pi$. The solid red lines correspond to the zero-admittance topological end modes and other lines correspond to the bulk modes. The parameters are set as follows: $C_1 = 0.6$ mF, $C_2 = 1$ mF, $C_4 = 0.5$ mF, $J = 1$ mF, and $N = 160$.

saddle point energies simultaneously approach each other. Until $C_5 = C_4$, these saddle point energies coalesce on the real axis in Fig. 3(b), which implies the coalescence of the ends of the OBC spectrum, corresponding to the degeneracy of all eigenstates into the two states with $E = \pm C_1$ on the complex plane. The degenerate point can be considered a type of higher-order exceptional point, which can characterize non-Bloch \mathcal{PT} -symmetry broken phase [51],

$$E(\beta_{S,i}) = E(\beta_{S,j}), \quad (13)$$

where $\beta_{S,(i,j)}$ represents saddle points belonging to the GBZ. In Fig. 3(c), as C_5 continues to increase, the two pairs of saddle points separate from each other with S_1 (S_3) moving upward and S_2 (S_4) moving downward, which leads to the occurrence of complex eigenvalues corresponding to non-Bloch \mathcal{PT} -symmetry breaking.

The coalescence of saddle point energies is associated with $\beta_{S,(i,j)}$. As shown in Figs. 3(d)–3(f), we calculate the GBZ and find that it consistently appears as a circle; its radius is the absolute value of the similarity coefficient $|r|$ in Eq. (6). Additionally, one can see that the saddle points within the GBZ, and their corresponding energies, are situated along the imaginary axis on the complex energy plane. However, since these saddle points are not on the GBZ, the corresponding energies of the saddle points do not exhibit any correlation with the behavior of the system. In Fig. 3(d), the saddle points $\beta_{S,2}$ and $\beta_{S,3}$ coalesce, appearing at the leftmost point in the GBZ, the saddle points $\beta_{S,1}$ and $\beta_{S,4}$ appear at the rightmost point in the GBZ. With the increase of C_5 , the radius of the GBZ decreases, and the saddle points $\beta_{S,(1,4)}$ and $\beta_{S,(2,3)}$

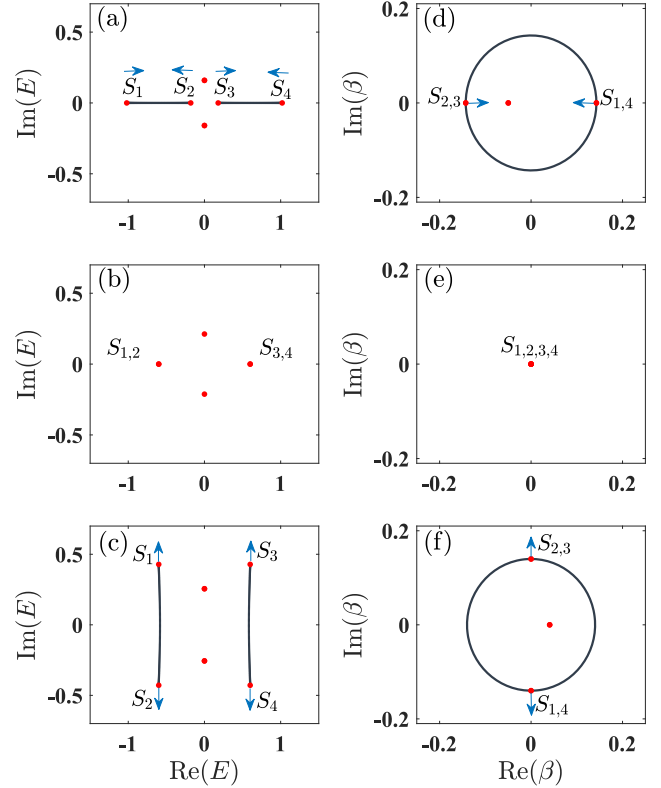


FIG. 3. Admittance spectrum on complex plane and the motion of saddle point energies with (a) $C_5 = 0.48$ mF, (b) $C_5 = 0.5$ mF, and (c) $C_5 = 0.52$ mF. Transition of the GBZ and saddle points with (d) $C_5 = 0.48$ mF, (e) $C_5 = 0.5$ mF, and (f) $C_5 = 0.52$ mF. The red solid dots represent saddle points and the parameters are $C_1 = 0.6$ mF, $C_2 = 1$ mF, $C_4 = 0.5$ mF, and $N = 160$.

move closer to the center of the circle. As shown in Fig. 3(e), when $C_5 = C_4$, the GBZ shrinks to a single point, implying that all saddle points coalesce. Solving $f(\beta, E)$ confirms the coalescence of the saddle point energies and the non-Bloch \mathcal{PT} -symmetry broken phase. In Fig. 3(f), as C_5 continues to increase, the saddle points $\beta_{S,(1,4)}$ and $\beta_{S,(2,3)}$ separate from each other. Noticing that when $C_5 = -C_4$, the radius of the GBZ $|r| \rightarrow \infty$, we cannot observe the coalescence of $\beta_{S,(1,4)}$ and $\beta_{S,(2,3)}$ because all of them are located at infinity, but we still can observe the saddle point energies collapsing, $E(\beta_{S,(1,4)}) = E(\beta_{S,(2,3)})$. Therefore, we can obtain the phase boundary of non-Bloch \mathcal{PT} symmetry given by

$$|C_5| = C_4. \quad (14)$$

To further analyze the non-Bloch \mathcal{PT} -symmetry transition of the system, the ratio of the complex eigenenergies is considered, which is defined as [4]

$$f_{\text{Im}} = \frac{D_{\text{Im}}}{D}, \quad (15)$$

where D_{Im} is the number of imaginary eigenvalues, and D is the total number of eigenvalues. Here, a cutoff of $T = 10^{-13}$ is used, and $|\text{Im}(E)| > T$ is identified to be a machine error. As shown in Fig. 4, we show the numerical solution of f_{Im} as a function of θ and C_4 . The black region of the phase diagram corresponds to the non-Bloch \mathcal{PT} -symmetry unbroken phase

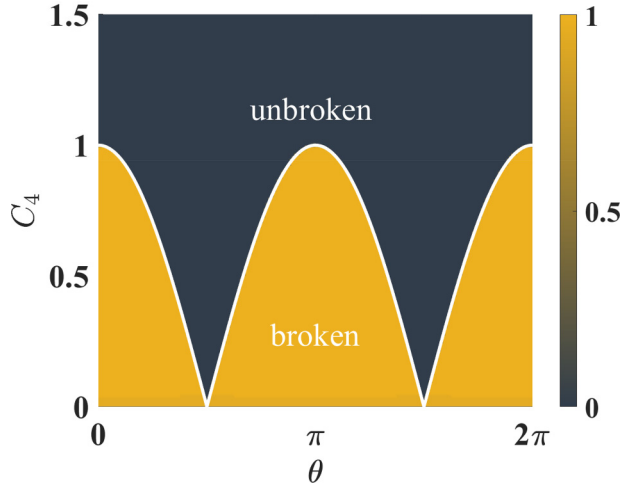


FIG. 4. Non-Bloch \mathcal{PT} -symmetry phase diagram. The black and yellow regions represent the non-Bloch \mathcal{PT} -symmetry unbroken and broken phases, and the white line is the phase boundary determined by Eq. (14). The parameters are same as those in Fig. 3.

with $f_{\text{Im}} = 0$, where the eigenvalues of the system are purely real. The yellow region of the phase diagram corresponds to the non-Bloch \mathcal{PT} -symmetry broken phase, where the energy eigenvalues of the system occurs complex values. The phase boundary between the two phases is indicated by the white solid line in Fig. 4, which can be fitted by Eq. (14). We find the phase boundary of non-Bloch \mathcal{PT} symmetry depends only on long-range coupling strengths C_4 and C_5 , which implies that the non-Bloch \mathcal{PT} -symmetry broken and unbroken phases will not change as coupling strengths C_1 and C_2 vary.

B. Topological phase transition for $C_2 > C_4$

In this subsection, we investigate the topological properties of the system with the strength relations $C_2 > C_4$. From the admittance spectra in Figs. 2(a) and 2(b), it is evident that the zero-admittance end modes, represented by solid red lines, are present in the topological nontrivial regions of $\theta \in (0, 0.21\pi) \cup \theta \in (0.35, 0.65\pi) \cup (0.79\pi, 1.21\pi) \cup (1.35\pi, 1.65\pi) \cup (1.79\pi, 2\pi)$. Moreover, to represent the localization properties of these zero-admittance end modes, we plot the node voltage density distribution of the system, as shown in Figs. 2(c)–2(f). We find that the zero-admittance topological end modes are localized at the left boundary of the system when $\theta \in (0, 0.5\pi)$ in Figs. 2(c) and 2(d). In contrast, the zero-admittance topological end modes are localized at the right boundary of the system when $\theta \in (0.5\pi, \pi)$ in Figs. 2(e) and 2(f). Note that the node voltage density distribution of the system shows mirror symmetry about $\theta = \pi$.

Obviously, the emergence of the zero-admittance end modes indicates the topological phase transition of the system. To precisely display the phase transition properties, we show the phase diagram of the system by introducing the non-Bloch winding number. The non-Hermitian Hamiltonian $H(k)$ can

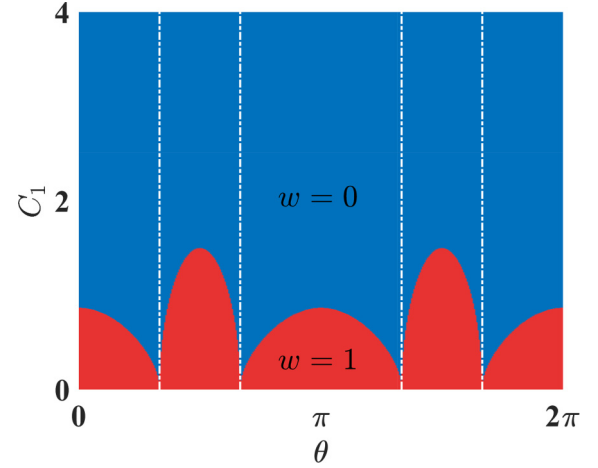


FIG. 5. Topological winding number on the C_1 - θ plane. The red and blue regions represent the topological nontrivial phase with $w = 1$ and the trivial phase with $w = 0$, respectively. The parameters are the same as those in Fig. 2.

be rewritten as

$$\begin{aligned} H(\beta) &= h_+(\beta)\sigma_+ + h_-(\beta)\sigma_-, \\ h_+(\beta) &= C_1 + (C_2 - C_3)\beta^{-1} + (C_4 + C_5)\beta, \\ h_-(\beta) &= C_1 + (C_2 + C_3)\beta + (C_4 - C_5)\beta^{-1}, \end{aligned} \quad (16)$$

where $\sigma_{\pm} = (\sigma_x \pm i\sigma_y)/2$. After solving the eigenvalue equation $|H(\beta) - E| = 0$, there exist four different eigenenergies $\beta_N(E)$. All the middle two solutions $|\beta_2(E)| = |\beta_3(E)|$ form the generalized Brillouin zone \mathcal{C}_β [26]. The corresponding winding number is defined as

$$w = \frac{i}{2\pi} \oint_{\mathcal{C}_\beta} dq q^{-1}(\beta), \quad (17)$$

where $q(\beta) = \sqrt{h_+(\beta)/h_-(\beta)}$ and $q^{-1}(\beta) = \sqrt{h_-(\beta)/h_+(\beta)}$. The winding number w is a useful tool for characterizing topological properties. In the context of the GBZ theory framework, we calculate the winding number w to distinguish between topologically trivial and nontrivial regions. As shown in Fig. 5, we plot the winding number phase diagram of the system versus C_1 and θ with $C_2 = 1$ mF, $C_4 = 0.5$ mF, and $N = 160$. It is found that the current system exhibits the two phase regions. The red region represents the topologically nontrivial phase with $w = 1$ and the blue region denotes the topologically trivial phase with $w = 0$. The white lines represent the phase boundary of non-Bloch \mathcal{PT} symmetry. We find that the system undergoes the topological phase transition in both the non-Bloch \mathcal{PT} -symmetry broken and unbroken phases. Notably, the system represents the transition from the topologically nontrivial phase from $w = 1$ to the topologically trivial phase $w = 0$.

C. Topological phase transition for $C_2 < C_4$

In this subsection, we further analyze the topological properties for $C_2 < C_4$. As shown in Figs. 6(a) and 6(b), we plot the admittance spectrum as a function of θ under the OBC with $C_1 = 0.4$ mF, $C_2 = 0.2$ mF, $C_4 = 0.5$ mF, and $N = 160$. One can see that the zero-admittance gap modes,

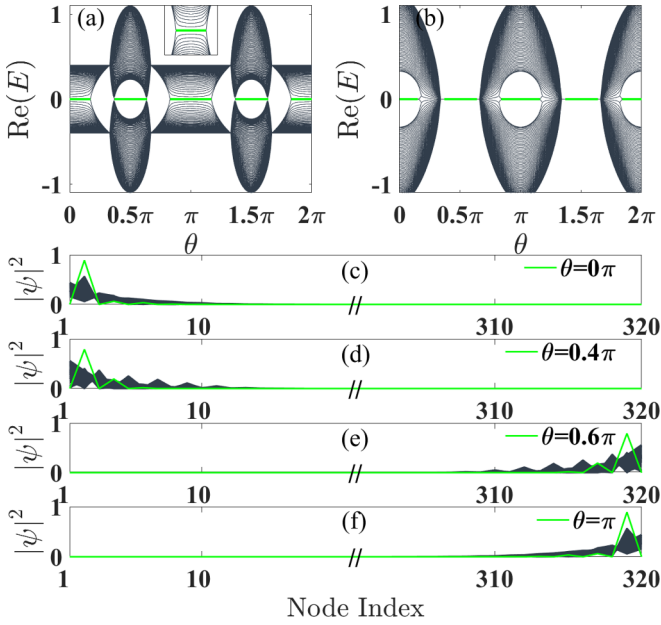


FIG. 6. Admittance spectrum of H as a function θ under the OBC with real (a) and imaginary (b) spectra. Node voltage density distribution of the system with (c) $\theta = 0$, (d) $\theta = 0.4\pi$, (e) $\theta = 0.6\pi$, and (f) $\theta = \pi$. The solid green lines correspond to the zero-admittance topological gap modes and other lines correspond to the bulk modes. The parameters are set as follows: $C_1 = 0.4$ mF, $C_2 = 0.2$ mF, $C_4 = 0.5$ mF, $J = 1$ mF, and $N = 160$.

represented by solid red lines, are present in the topologically nontrivial regions of $\theta \in (0, 0.19\pi) \cup (0.37, 0.63\pi) \cup (0.81\pi, 1.19\pi) \cup (1.37\pi, 1.63\pi) \cup (1.81\pi, 2\pi)$. We also plot the node voltage density distribution of these zero-admittance topological gap modes, as shown in Figs. 6(c)–6(f). We find that the gap modes are respectively localized at the second and penultimate sites of the system with $\theta \in (0, 0.5\pi)$ and $\theta \in (0.5\pi, 1\pi)$, which is significantly different with previous analyzed end modes for $C_2 > C_4$.

In order to visually display the topological phase transition for $C_2 < C_4$, we plot the winding number phase diagram of the system versus C_1 and θ with $C_2 = 0.2$ mF and $C_4 = 0.5$ mF, as shown in Fig. 7. We find that the current system also exhibits the two phase regions. The green and blue regions represent the topologically nontrivial phase $w = -1$ and the topologically trivial phase $w = 0$, respectively. The white lines represent the non-Bloch \mathcal{PT} -symmetry phase boundary. We find that the system undergoes the topological phase transition in both the non-Bloch \mathcal{PT} -symmetry broken and unbroken phases. While the topological phase transition occurs between the winding numbers $w = -1$ and $w = 0$. Moreover, the current system holds zero-admittance topological gap modes with $w = -1$, which is a significant difference compared to Fig. 5.

IV. CONCLUSIONS

In conclusion, we have investigated the 1D non-Hermitian Su-Schrieffer-Heeger model with long-range hopping using

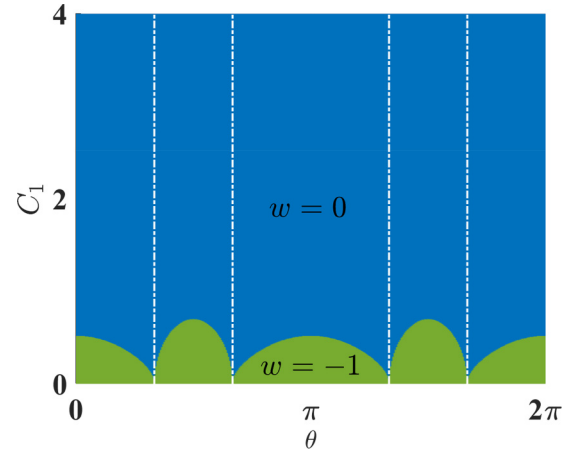


FIG. 7. Topological winding number on the C_1 - θ plane. The green region represents topological nontrivial phases $w = -1$, and the blue region represents the topological trivial phase with $w = 0$. The parameters are same as those in Fig. 6.

the electrical circuit system consisting of capacitors, inductors, and operational amplifiers. Our analysis focuses on the non-Bloch \mathcal{PT} -symmetry unbroken and broken phases of the system, which can be illustrated using the saddle point theory. Notably, the phase boundary of the non-Bloch \mathcal{PT} symmetry only depends on the long-range coupling strengths C_4 and C_5 . When $|C_5| > C_4$, the non-Bloch \mathcal{PT} symmetry is broken, and when $|C_5| < C_4$, the non-Bloch \mathcal{PT} symmetry is unbroken. We determined the non-Bloch \mathcal{PT} -symmetry phase boundary by considering the ratio of complex eigenenergy. Furthermore, we have observed the emergence of zero-admittance topological end modes and gap modes, which depend on the relative magnitudes of the hopping strengths C_2 and C_4 . When $C_2 > C_4$, a topological phase transition occurs in both the non-Bloch \mathcal{PT} -symmetry unbroken and broken regions, resulting in a winding number change from $w = 1$ to $w = 0$. Additionally, the topological zero-admittance end modes are localized at the first (or last) site. On the other hand, when $C_2 < C_4$, the system undergoes a topological phase transition with a winding number change from $w = -1$ to $w = 0$, and the topological zero-admittance gap modes are localized at the second (or penultimate) site. This work presents a method to implement nonreciprocal topoelectrical circuits and contributes to a deeper understanding of the interplay between topology and non-Hermiticity.

ACKNOWLEDGMENTS

This work was supported by the National Natural Science Foundation of China under Grants No. 62301472, No. 12375020, No. 12074330, and No. 62071412; the Natural Science Foundation of Jilin Province under Grant No. YDZJ202201ZYTS298; the Education Department of Jilin Province under Grant No. JJKH20220530KJ; and the Young Talents Support Project of Association of Science and Technology of Jilin Province under Grant No. QT2021029.

- [1] S. Longhi, *Phys. Rev. Lett.* **103**, 123601 (2009).
- [2] S. Malzard, C. Poli, and H. Schomerus, *Phys. Rev. Lett.* **115**, 200402 (2015).
- [3] L. Z. Tang, G. Q. Zhang, L. F. Zhang, and D. W. Zhang, *Phys. Rev. A* **103**, 033325 (2021).
- [4] C. Wu, N. Liu, G. Chen, and S. Jia, *Phys. Rev. A* **106**, 012211 (2022).
- [5] X. D. Zhao, Y. Xing, L. Qi, S. T. Liu, S. Zhang, and H. F. Wang, *New J. Phys.* **23**, 073043 (2021).
- [6] S. Longhi, *Phys. Rev. B* **81**, 195118 (2010).
- [7] S. Longhi, *Phys. Rev. B* **82**, 041106(R) (2010).
- [8] H. Cao and J. Wiersig, *Rev. Mod. Phys.* **87**, 61 (2015).
- [9] S. Diehl, E. Rico, M. A. Baranov, and P. Zoller, *Nat. Phys.* **7**, 971 (2011).
- [10] H. J. Carmichael, *Phys. Rev. Lett.* **70**, 2273 (1993).
- [11] T. E. Lee and C. K. Chan, *Phys. Rev. X* **4**, 041001 (2014).
- [12] M. Papaj, H. Isobe, and L. Fu, *Phys. Rev. B* **99**, 201107(R) (2019).
- [13] T. Yoshida, R. Peters, and N. Kawakami, *Phys. Rev. B* **98**, 035141 (2018).
- [14] P. A. McClarty and J. G. Rau, *Phys. Rev. B* **100**, 100405(R) (2019).
- [15] B. Bahari, A. Ndao, F. Vallini, A. E. Amili, Y. Fainman, and B. Kanté, *Science* **358**, 636 (2017).
- [16] M. Parto, S. Wittek, H. Hodaei, G. Harari, M. A. Bandres, J. Ren, M. C. Rechtsman, M. Segev, D. N. Christodoulides, and M. Khajavikhan, *Phys. Rev. Lett.* **120**, 113901 (2018).
- [17] L. Feng, Z. J. Wong, R. M. Ma, Y. Wang, and X. Zhang, *Science* **346**, 972 (2014).
- [18] H. Hodaei, M. A. Miri, M. Heinrich, D. N. Christodoulides, and M. Khajavikhan, *Science* **346**, 975 (2014).
- [19] W. X. Cui, L. Qi, Y. Xing, S. T. Liu, S. Zhang, and H. F. Wang, *Opt. Express* **28**, 37026 (2020).
- [20] C. E. Rüter, K. G. Makris, R. El-Ganainy, D. N. Christodoulides, M. Segev, and D. Kip, *Nat. Phys.* **6**, 192 (2010).
- [21] D. C. Brody, *J. Phys. A* **47**, 035305 (2014).
- [22] W. D. Heiss, *J. Phys. A: Math. Theor.* **45**, 444016 (2012).
- [23] M. A. Miri and A. Alú, *Science* **363**, eaar7709 (2019).
- [24] J. H. Dong, Q. M. Hu, C. Y. Ji, B. S. Zou, and Y. Y. Zhang, *New J. Phys.* **23**, 113025 (2021).
- [25] S. Rafi-Ul-Islam, Z. B. Siu, and M. B. Jalil, *New J. Phys.* **23**, 033014 (2021).
- [26] S. Yao and Z. Wang, *Phys. Rev. Lett.* **121**, 086803 (2018).
- [27] S. Yao, F. Song, and Z. Wang, *Phys. Rev. Lett.* **121**, 136802 (2018).
- [28] F. Song, S. Yao, and Z. Wang, *Phys. Rev. Lett.* **123**, 170401 (2019).
- [29] F. Song, S. Yao, and Z. Wang, *Phys. Rev. Lett.* **123**, 246801 (2019).
- [30] K. Zhang, Z. Yang, and C. Fang, *Phys. Rev. Lett.* **125**, 126402 (2020).
- [31] C. H. Lee and R. Thomale, *Phys. Rev. B* **99**, 201103(R) (2019).
- [32] L. Jin and Z. Song, *Phys. Rev. B* **99**, 081103(R) (2019).
- [33] L. Herviou, J. H. Bardarson, and N. Regnault, *Phys. Rev. A* **99**, 052118 (2019).
- [34] H. Jiang, C. Yang, and S. Chen, *Phys. Rev. A* **98**, 052116 (2018).
- [35] W. Brzezicki and T. Hyart, *Phys. Rev. B* **100**, 161105(R) (2019).
- [36] K. Yokomizo and S. Murakami, *Phys. Rev. Lett.* **123**, 066404 (2019).
- [37] F. K. Kunst, E. Edvardsson, J. C. Budich, and E. J. Bergholtz, *Phys. Rev. Lett.* **121**, 026808 (2018).
- [38] S. Longhi, *Phys. Rev. Res.* **1**, 023013 (2019).
- [39] G. F. Guo, X. X. Bao, and L. Tan, *New J. Phys.* **23**, 123007 (2021).
- [40] T. Zhang, X. Zhang, M.-H. Lu, and Y.-F. Chen, *Phys. Rev. B* **107**, 094111 (2023).
- [41] H. Xin, W. Song, S. Wu, Z. Lin, S. Zhu, and T. Li, *Phys. Rev. B* **107**, 165401 (2023).
- [42] J. Q. Li, J. J. Li, L. Qi, Z. X. Zhang, J. Cao, W. X. Cui, S. Zhang, and H. F. Wang, *Ann. Phys. (Berlin)* **535**, 2300133 (2023).
- [43] Z. Yang, K. Zhang, C. Fang, and J. Hu, *Phys. Rev. Lett.* **125**, 226402 (2020).
- [44] C.-C. Liu, L.-H. Li, and J. An, *Phys. Rev. B* **107**, 245107 (2023).
- [45] T. Li, J.-Z. Sun, Y.-S. Zhang, and W. Yi, *Phys. Rev. Res.* **3**, 023022 (2021).
- [46] K. Xu, X. Zhang, K. Luo, R. Yu, D. Li, and H. Zhang, *Phys. Rev. B* **103**, 125411 (2021).
- [47] L. Qi, A. L. He, H. F. Wang, and Y. Liu, *Phys. Rev. B* **107**, 115107 (2023).
- [48] M. J. Colbrook, B. Roman, and A. C. Hansen, *Phys. Rev. Lett.* **122**, 250201 (2019).
- [49] T. E. Lee, *Phys. Rev. Lett.* **116**, 133903 (2016).
- [50] D. Leykam, K. Y. Bliokh, C. Huang, Y. D. Chong, and F. Nori, *Phys. Rev. Lett.* **118**, 040401 (2017).
- [51] Y. M. Hu, H. Y. Wang, Z. Wang, and F. Song, *Phys. Rev. Lett.* **132**, 050402 (2024).
- [52] W. X. Cui, Y. Xing, L. Qi, X. Han, S. T. Liu, S. Zhang, and H. F. Wang, *Opt. Express* **28**, 13532 (2020).
- [53] T. Helbig, T. Hofmann, C. H. Lee, R. Thomale, S. Imhof, L. W. Molenkamp, and T. Kiessling, *Phys. Rev. B* **99**, 161114(R) (2019).
- [54] S. Rafi-Ul-Islam, Z. B. Siu, and M. B. Jalil, *Appl. Phys. Lett.* **116**, 111904 (2020).
- [55] S. M. Rafi-Ul-Islam, Zhuo Bin Siu, and M. B. A. Jalil, *Phys. Rev. B* **103**, 035420 (2021).